

1 **Revision 1**

2 ***Ab initio* calculations and crystal structure simulations for mixed layer**
3 **compounds from the tetradymite series**

4 **JIE YAO^{1*}, CRISTIANA L. CIOBANU¹, NIGEL J. COOK¹, KATHY EHRIG^{1,2},**
5 **GABRIEL I. DIMA^{3,4}, GERD STEINLE-NEUMANN⁵**

6 ¹School of Chemical Engineering, The University of Adelaide, Adelaide S.A. 5005, Australia

7 ²BHP Olympic Dam, 10 Franklin Street, Adelaide S.A. 5000, Australia

8 ³Cooperative Institute for Research in Environmental Sciences (CIRES), CU Boulder, CO 80309, USA

9 ⁴NOAA National Centers for Environmental Information (NCEI), DSRC, 325 Broadway, Boulder, CO
10 80305, USA

11 ⁵Bayerisches Geoinstitut, University of Bayreuth, 95440 Bayreuth, Germany

12 **ABSTRACT**

13 Density functional theory (DFT) is used to obtain structural information of seven members of the
14 tetradymite homologous series: Bi₂Te₃ (tellurobismuthite), BiTe (tsumoite), Bi₄Te₃ (pilsenite), Bi₅Te₃,
15 Bi₂Te, Bi₇Te₃ (hedleyite) and Bi₈Te₃. We use the formula S(Bi_{2k}Te₃)•L[Bi_{2(k+1)}Te₃] as a working model
16 (k=1-4) where S and L are short and long modules in the structures. The relaxed structures show an
17 increase in the *a* parameter and decrease in the interlayer distance (*d_{sub}*) from Bi₂Te₃ (2.029 Å) to Bi₈Te₃
18 (1.975 Å). DFT-derived formation energy for each phase indicates they are all thermodynamically stable.
19 Scanning transmission electron microscopy (STEM) simulations for each of the relaxed structures show
20 an excellent match with atom models. Simulated electron diffractions and reflection modulation along
21 *c** are concordant with published data, where they exist, and with the theory underpinning mixed-layer
22 compounds. Two modulation vectors, $\mathbf{q}=\gamma \cdot \mathbf{c}_{sub}^*$ ($\gamma=1.800-1.640$) and $\mathbf{q}_F=\gamma_F \cdot \mathbf{d}_{sub}^*$ ($\gamma_F=0.200-0.091$),

23 describe the distribution of reflections and their intensity variation along $d_{sub}^* = 1/d_{sub}$. The γ_F
24 parameter reinforces the concept of $Bi_{2k}Te_3$ and $Bi_{2(k+1)}Te_3$ blocks in the double module structures and γ
25 relates to d_{sub} variation. Our model describing the relationship between γ and d_{sub} allows prediction of
26 d_{sub} beyond the compositional range considered in this study, showing that phases with $k > 5$ have
27 d_{sub} values within the analytical range of interlayer distance in bismuth. This in turn allows us to
28 constrain the tetradymite homologous series between γ values of 1.800 (Bi_2Te_3) and 1.588 ($Bi_{14}Te_3$).
29 Phase compositions with higher Bi/Te should be considered as disordered alloys of bismuth. These
30 results have implications for mineral systematics and classification as they underpin predictive models
31 for all intermediate structures in the group and can be equally applied to other mixed-layer series. Our
32 structural models will also assist in understanding variation in the thermoelectric and topological
33 insulating properties of new compounds in the broader tetradymite group and can support experimental
34 work targeting a refined phase diagram for the system Bi-Te.

35 Keywords: *tetradymite series, mixed layer compounds, crystal structure, Density Functional Theory,*
36 *STEM simulations*

37 INTRODUCTION

38 The tetradymite series [generally $Bi_x(Te, Se, S)_y$; where Te, Se, S are chalcogens] comprises phases
39 with crystal structures derived from the tetradymite archetype [Bi_2Te_2S , a 5-atom-thick layer, ‘mod5’]
40 (Cook et al. 2007, and references therein). Ciobanu et al. (2009) considers the tetradymite series a “metal-
41 or Bi-rich” series within a larger group of phases derived from the same tetradymite archetype. For the
42 sake of simplicity and the purpose of this contribution, we chose Te as the only chalcogen. There are two
43 models describing crystal structure modularity within the Bi-rich series (or tetradymite series *sensu*
44 *stricto*). The first, proposed by Imamov and Semiletov (1971), considers the combination of Bi_2 and
45 Bi_2Te_3 blocks (hereafter referred to as the “Mod2 and 5 model”), later formalised as $nBi_2 \cdot mBi_2Te_3$ by

46 Shelimova et al. (2000). The second model was introduced by Amelinckx et al. (1989) and Frangis et al.
47 (1990) as 5- and 7-layer lamellae based upon the electron diffraction properties indicating one
48 dimensional, interface modulated mixed layer compounds. This was subsequently formalised by Ciobanu
49 et al. (2009) for modules of incremental thickness, as an accretional homologous series with formula:
50 $S(\text{Bi}_{2k}\text{Te}_3) \cdot L[\text{Bi}_{2(k+1)}\text{Te}_3]$, where S and L are the number of short and long modules, respectively. This
51 model allows for definition of building modules with incremental thickness extending from module 5 to
52 7, 9, 11, and so on. These modules have a fixed number of chalcogen atoms and are incrementally
53 enriched in Bi, i.e., Bi_4Te_3 (7), Bi_6Te_3 (9), Bi_8Te_3 (11), relative to the 5-atom archetype, Bi_2Te_3 ,
54 explaining why this is referred to as the Bi-rich series.

55 Transmission electron microscopy (TEM) study of phases in the compositional range Bi_2Te_3 - Bi_8Te_3
56 are complemented by high angle annular dark field (HAADF) scanning TEM (STEM) studies of Bi_8Te_3
57 and $\text{Bi}_4(\text{Te,Se,S})_3$ that show the correlation between composition and structural modulation (Ciobanu et
58 al. 2009, 2021; Cook et al. 2021). Diffraction patterns show that all phases are N-fold superstructures (N
59 = layers in the stacking sequence) of a rhombohedral subcell with $c/3 = d_0 \sim 2.000 \text{ \AA}$. The structures are
60 characterised by two modulation vectors showing monotonic decrease in d-subcell (d_{sub}) with
61 increasing Bi composition.

62 Several named minerals and other unnamed phases in the tetradyte group are reported from natural
63 assemblages, particularly from gold deposits (Cook et al. 2007; 2009; Ciobanu et al. 2010) yet
64 remarkably few have been subject to crystal structure determination or crystallographic information data
65 file (cif). Compounds from this series are intensely studied for their thermoelectric and/or topological
66 insulating properties (Bos et al., 2007; 2012; Goldsmid, 2014). To better understand the series, we
67 perform *ab initio* calculations and structure simulations for phases with single and double modules across
68 the compositional range Bi_2Te_3 to Bi_8Te_3 (k=1-4). We use simulations of images and electron diffraction
69 patterns to assess the validity of the accretional model versus the “Mod 2 and 5” model and apply the

70 formation energies to evaluate phase stability of the seven phases. The determined crystal structure
71 parameters are used to develop a model for the series that involves variation in d_{sub} relative to
72 modulation.

73 **Crystal structure data and selection of input files**

74 Table 1 indicates the phases under consideration and published information on their crystal
75 structures. The symmetry and the number of layers in each structure can be derived from the explicit
76 chemical formula given by Ciobanu et al. (2009). In the present work, four structures with $S=1$, $L=0$, and
77 $k=1, 2, 3, 4$ (Bi_2Te_3 , Bi_4Te_3 ; Bi_6Te_3 and Bi_8Te_3), and three structures with $S=1$, $L=1$, and $k=1, 2, 3$
78 (Bi_6Te_6 ; $\text{Bi}_{10}\text{Te}_6$ and $\text{Bi}_{14}\text{Te}_6$) are included. These correspond to single and double module structures: (i)
79 5, 7, 9 and 11; and (ii) combinations of these with notation 5.7, 7.9 and 9.11, respectively. The number
80 of layers in the asymmetric unit cell is $N_1=S(2k+3)+L(2k+5)$. If the number of atoms in the explicit
81 formula is divisible by 3, as in the case of Bi_6Te_6 (BiTe , tsumoite) and Bi_6Te_3 (unnamed Bi_2Te), the
82 symmetry changes from $R\bar{3}m$ (hereafter called R) to $P\bar{3}m1$ (hereafter called H). The total number of
83 layers in the structure is $N=N_1 \times 3$ for R phases and $N = N_1$ for H phases. Knowing that the distance
84 between two consecutive layers (Imamov and Semiletov 1971), the ideal d_0 , approximates to 2.000 Å,
85 we can calculate the c parameter using the formula: $c = N_1 \times 2.000 \text{ \AA}$.

86 We selected 12 published crystal structures for the phases targeted here that have been documented
87 from x-ray powder or single crystal diffraction studies, and two from (S)TEM data (Table 2). Published
88 data are unevenly distributed among the seven phases. For example, there are five studies of Bi_2Te_3
89 (tellurobismuthite) but no x-ray diffraction studies for either Bi_5Te_3 or Bi_8Te_3 . Most of the published
90 studies were carried out on synthetic material and only a single study was performed on natural
91 tellurobismuthite (Nakajima 1962), highlighting the difficulty in finding natural material suitable for
92 crystal structure determination of these phases. We observe that a increases slightly from Bi_2Te_3 to
93 Bi_8Te_3 whereas the c parameter varies widely as it is dependent upon N and symmetry. However, using

94 the c parameter we can calculate the variation in the interlayer distance defining the subcell from which
95 the layers are derived (d_{sub}). This interval, calculated from analytical measurements, shows a decrease
96 from ~ 2.000 Å to 1.910 Å across the Bi_2Te_3 - Bi_8Te_3 range, with some fluctuations (Table 1).

97 METHODS

98 **Ab initio calculations**

99 To explore the correlation between crystal structural modularity and chemical variation in a series
100 of mixed-layer compounds, we have employed *ab initio* total energy calculations and structure relaxation
101 using density functional theory (DFT) (Hohenberg and Kohn 1964; Kohn and Sham 1965). Input data
102 for structure optimisation comprised crystallographic information files (cif) from the literature (Table 1).
103 An exception was the Bi_5Te_3 phase, for which a predicted structure was obtained using CrystalMaker
104 (CM) (Palmer 2015) and Findsym software (Stokes and Hatch 2005).

105 The DFT calculations were performed with the Vienna *ab initio* simulation package (VASP) (Kresse
106 and Furthmüller 1996; Kresse and Joubert 1999), using the projector augmented wave (PAW) method
107 (Blöchl 1994). A plane wave basis set with energy cut-off of 500 eV was employed for all calculations.
108 The electronic exchange and correlation energy were estimated by the generalized gradient
109 approximation (GGA) with Perdew, Burke and Ernzerhof (PBE) parameters (Perdew et al. 1996). We
110 included van der Waals interactions between atoms of the same type (Te-Te and Bi-Bi) using the method
111 of Grimme et al. (2010), which adds a small dispersion energy correction to the total energy in the system.
112 This is also shown in a recent publication in which the electronic structure of Bi_4Te_3 phase is predicted
113 to be a semimetal (Nabok et al., 2022).

114 The Brillouin zone (BZ) was sampled at Γ -centred dense k-point grids based on the Monkhorst-Pack
115 scheme (Pack and Monkhorst 1977). The set of k-points was considered dependent upon the cell

116 parameters and symmetry of each structure (Table 1) to maximize the total energy accuracy while aiming
117 to minimize computational cost.

118 Volumes from each input file were considered as V_i for each structure. The lattice parameters (a , c)
119 in each case were subsequently scaled in the range 95 to 101% to obtain a series of volume values. For
120 consistency, the volume relaxation was performed at constant energy cut-off. Total energy calculations
121 and structural optimization for the atomic positions and cell parameters (c and a) were carried out for
122 individual volumes with energy tolerance $<10^{-5}$ eV between two ionic steps and force less than 0.02 eV/Å
123 per atom. After volume relaxation, a static calculation is performed to obtain the total energy at each
124 volume.

125 To obtain the equilibrium volume and ground state energy we used the Murnaghan (1944) equation
126 of state (EOS) as being most appropriate for compounds with trigonal symmetry (e.g. the same EOS used
127 by other studies of Bi-tellurides; Nakayama et al. 2009). The Birch-Murnaghan (1947) EOS was
128 introduced for phases with cubic symmetry. Equilibrium volume and ground state energy were found by
129 fitting the Murnaghan (Murnaghan 1944) equation of state (EOS):

130
$$E(V) = E_0 + \frac{K_0 V}{K'_0} \left(\frac{(V_0/V)^{K'_0}}{K'_0 - 1} + 1 \right) - \frac{K_0 V_0}{K'_0 - 1}, \quad (1)$$

131 where K_0 and K'_0 are the bulk modulus and its pressure derivative, V_0 represents the equilibrium volume
132 and E_0 is the reference energy. The calculated parameters after EOS fitting are given in Table 3. The
133 optimized lattice parameters for each structure were obtained by performing relaxation at the
134 corresponding equilibrium volume.

135 **Crystal structure models**

136 All the relaxed crystal structures were modelled and assessed using CM and Findsym was used to
137 generate the cif data files. Electron diffractions and STEM image simulation were performed using

138 HREM STEM software for structure visualization. A computer subroutine was written in Python for
139 intensity calculations and simulations of reflections.

140 RESULTS

141 Crystal structure relaxation

142 We have selected six of the structures given in Table 1 as a basis for crystallographic file input (cif)
143 in the DFT calculations. For Bi_5Te_3 we use experimental parameters given by Ciobanu et al. (2009) and
144 obtain atom coordination by applying $1/N_1 = 1/16$ derived from the 7.9 modular structure with equal
145 intervals along the c direction for the z coordinates.

146 To constrain the seven crystal structures, we determined the equilibrium volume for each phase
147 (Figure 1) by fitting the total energy volume curves using equation (1), with the minimum well
148 constrained. The equilibrium volumes and EOS parameters are listed and compared with published data
149 in Table 3.

150 The fitted volumes are within 2% of the reference structures, except for Bi_8Te_3 for which the
151 difference is 9%. The main reason is that the parameters for this were obtained from S/TEM data which
152 carries a higher uncertainty. Our calculated bulk moduli (K_0) range from 33-40 GPa, concordant with
153 studies of elastic properties using *ab initio* calculations of bismuth-based alloys (Woodcox et al. 2019).
154 This is seen from a comparison for phases with the same composition, e.g., 40 GPa vs. 41 GPa (Woodcox
155 et al. 2019) for BiTe , as well as from the small variation of K_0 across the compositional range.

156 After the fitting step we calculated the structure parameters at V_0 (Table 4), with differences of $\pm 1\%$
157 for a and c relative to most reference structures, although differences were higher (a few %) for Bi_5Te_3
158 and Bi_8Te_3 . Comparable discrepancies between DFT calculations and input files for a crystal structure
159 are reported in other studies, e.g., for Bi_2Te_3 (Cheng and Ren 2011).

160 We also note that after relaxation, the a parameter is expanded whereas c contracts relative to the
161 input data (Tables 1 and 4). The comparison of the a parameter with published data (Figure 2a) shows
162 that relaxed structures follow a smooth trend, increasing with Te content across the range Bi_2Te_3 to
163 Bi_8Te_3 , with values systematically larger – by a small amount – than published measurements (Table 1).
164 An appreciation of published DFT data (Cheng and Ren, 2011) relative to analytical data is shown for
165 tellurobismuthite (Bi_2Te_3), the most intensively studied of the seven structures. Our data plots close to
166 the mean of published DFT data; the TEM-based lattice parameter a is smaller than both analytical and
167 DFT curves (Figure 2a).

168 The calculated d_{sub} parameter from DFT data (range 1.975 to 2.029 Å) also follow a smooth trend,
169 although with an inverse trend compared to a , i.e., decreasing with Bi content (Figure 2b). This curve
170 shows a steep downwards slope from tellurobismuthite (Bi_2Te_3) to tsumoite (BiTe), followed by a gentle
171 decreasing trend intersecting the d_{sub} axis at ~ 1.960 Å for a 0 atom.% Te composition (native bismuth).
172 The analytical data is noisier, but generally consistent (Figure 2c). The largest difference occurs for Bi_2Te
173 between our DFT results and the XRD data by Bos et al. (2012) with 0.012 Å difference (1.2 %), if we
174 ignore the TEM data for Bi_8Te_3 , which differs from the present calculated range of d_{sub} by 0.050 Å
175 (Ciobanu et al. 2021). A good fit is obtained between DFT and the d_{sub} of Bi_2Te given by Zavylov et al.
176 (1976). Excellent agreement is obtained for tsumoite (BiTe) and tellurobismuthite (Bi_2Te_3) with data
177 from Yamana et al. (1979) and Atuchin et al. (2012), respectively.

178 To assess the differences between the DFT and experimental data we also undertook the PBEsol
179 functional method (Perdew et al., 2008). The results show that the for the endmember Bi_2Te_3 , its
180 interlayer distance d_{sub} is underestimated relative to experimental data (i.e., 3.1%) although it reduces
181 the difference to a parameter (i.e., 0.5%). In contrast, the chosen PBE functional method gives a better
182 fit with the analytical data for d_{sub} (i.e., 0.2%, and by inference for the c parameter), which is most
183 important for the topic addressed here.

184 **Models and simulations for the relaxed structures**

185 The relaxed structures were plotted as models on the $[11\bar{2}0]$ zone axis to show the incremental width
186 of the $2k+3$ modules and the bond topology across the range Bi_2Te_3 - Bi_8Te_3 (Figures 3 and 4). Crystal
187 structure models for any phase in the group can be obtained from generic atomic coordinate calculations
188 following the same approach applied here for phases without initial cif files (i.e., Bi_5Te_3 and hedleyite).
189 The bond topology in such models would be orthogonal whereas the optimized structures, either obtained
190 from measurements or DFT relaxation will show slight distortions (Figures 3 and 4; left column). The
191 structural modules are schematically shown using the accretional formalism $[\text{S}(\text{Bi}_{2k}\text{Te}_3)\bullet\text{L}(\text{Bi}_{2(k+1)}\text{Te}_3)]$,
192 but these are not necessarily constrained relative to models using the $n\text{Bi}_2\bullet m\text{Bi}_2\text{Te}_3$ formula. This is
193 particularly apparent for phases such as BiTe tsumoite where two Bi_2Te modules ($m=2$) are linked by
194 one Bi_2 block ($n=1$) (Figure 4, upper panel). The atom fill models are shown for purposes of comparison
195 with the STEM simulations in Section 4.4 (Figures 3 and 4; right column).

196 **Bond analysis**

197 Bond distances for atoms in the asymmetric unit cells are shown in Figures 5 and 6. A comparison
198 of the minimum and maximum bond lengths for each structure is given in Figure 7. All seven structures
199 contain Bi-Te bonds but only two have Te-Te bonds and only six have Bi-Bi bonds. The Te-Te bonds
200 are longer than all other bonds and virtually the same for tellurobismuthite (3.694 Å) and tsumoite (3.692
201 Å) (Figure 7b). The relative proportion of Bi-Bi versus Bi-Te bonds increases from 1/6 in pilsenite to 5/6
202 in Bi_8Te_3 when considering the neighbouring bonds (Figure 5). The double module structures all fall
203 within this range, except for tsumoite which has a Bi-Bi / Bi-Te ratio of 1/10 (Figure 6).

204 The minimum for Bi-Te bond lengths increases by ~ 0.027 Å, from tellurobismuthite (3.080 Å) to
205 Bi_8Te_3 (3.107 Å), but this is stepwise, with the largest difference between tsumoite and pilsenite and no
206 discernible difference between Bi_2Te and hedleyite (Figure 7a). The maximum Bi-Te bond lengths
207 increase sharply between tellurobismuthite and pilsenite (~ 0.303 Å) but decrease gently towards Bi_8Te_3

208 (Figure 7b). The minimum Bi-Bi bond lengths increase with Bi content, giving a relatively smooth curve
209 between tsumoite and Bi_8Te_3 with a difference of $\sim 0.013 \text{ \AA}$ (Figure 7c). The maximum Te-Te bond
210 lengths are significantly longer than the Bi-Bi bonds ($\sim 0.159 \text{ \AA}$; Figure 7d). In the four phases with more
211 than one Bi-Bi bond, the maximum Bi-Bi length tend to decrease with Bi content from Bi_5Te_3 to Bi_8Te_3 ,
212 but not continuously. Overall, minimum bond lengths show a consistent variation across the range
213 Bi_2Te_3 - Bi_8Te_3 , whereas the maximum is complicated by the presence of phases with Te-Te bonds (Figure
214 7). Bond lengths are important for understanding the variation of interlayer distances (d_{sub}), and the
215 analysis above indicates a strong split between phases that contain Te-Te bonds (larger d_{sub} values) and
216 those that do not.

217 **Simulation of STEM images and electron diffractions**

218 The relaxed structures are shown as simulations of STEM images and electron diffraction (ED)
219 patterns on the $[11\bar{2}0]$ zone axis in Figures 8 and 9. The images show a very good agreement with the
220 atom fill models on the same zone axis shown in Figures 3 and 4. The d_{sub} interval is also shown as two
221 simulations, one cropped from the ED patterns (upper strips) and a second one computed using the
222 displacement introduced by the fractional shift method of Amelinckx et al. (1989) and Frangis et al.
223 (1990) (lower strips) (see Ciobanu et al. 2009 for more details). The d_{sub}^* interval is important for
224 defining the modulation underpinning the increase in width of the modules. In this interval the number
225 of reflections (n_r) corresponds to N_1-1 , equally distributed along d_{sub}^* . The length of the asymmetric unit
226 cell (d_{N_1}) along c corresponds to the layer stacks defining each unit cell. This is also marked as the
227 smallest interval, $d_{N_1}^*$ between two adjacent reflections along d_{sub}^* . The d_{N_1} interval for the structures
228 with double modules (S, L=1) approximates to the sum of S and L lengths.

229 All ED patterns show the two brightest reflections about the middle of d_{sub}^* with monotonic decrease
230 of the interval between them as the Bi concentration increases. Two modulation vectors are shown for

231 each phase. The $\mathbf{q}=\gamma \cdot c_{sub}^*$ vector defined by Lind and Lidin (2003) is based on displacive modulation
232 between chalcogen (Te, Se, S) and Bi atoms, where q is the homoatomic interval. The \mathbf{q} modulation is
233 depicted up to third-order reflections along c^* (ED patterns in Figures 8 and 9). The γ values (1.800-
234 1.640 for the range Bi_2Te_3 - Bi_8Te_3) are calculated as $3 \cdot [(N_1+1)/2]/N_1$ for single modules (Figure 8) and
235 $3 \cdot [(N_1+2)/2]/N_1$ for double modules (Figure 9). The γ values correlate with the chemical formula by the
236 relation $\gamma=3[S(k+2)+L(k+3)]/N_1$. The same γ range was shown by Ciobanu et al (2009) as selected area
237 electron diffraction (SAED), and accompanying TEM images, for natural phases where an ideal
238 $d_{sub} \sim 2.000 \text{ \AA}$ was assumed. The relaxed structures presented here show excellent agreement with those
239 SAEDs. Here, however, the STEM image simulations complement the ED patterns. Such simulations,
240 reproducing the atom models, efficiently describe the nature of phases from the tetradymite group
241 documented in prior STEM studies, e.g., Medlin et al. 2014 for tellurobismuthite, Ciobanu et al. (2021)
242 for Bi_8Te_3 , and Cook et al., 2001 for $\text{Bi}_4(\text{Te,S,Se})_3$ phases.

243 The second modulation vector $q_F = \gamma_F \cdot d_{sub}^*$ and $q_F = i/N_1 \cdot d_{sub}^* = i \cdot d_{N_1}^*$ ($\gamma_F = i/N_1$; $i =$
244 $S + L$), introduced by Frangis et al (1990), relates changes in module size and their respective number to
245 displacements in the basic substructure. This is particularly instructive for depicting the correlation
246 between the building modules (S, L) and electron diffractions patterns. We show that the interval defined
247 by the two brightest reflections about the middle of d_{sub} can be divided into two for all the double module
248 structures (Figure 9). The intensity variation along d_{sub}^* is simulated using the fractional shift method
249 following the adapted \mathbf{q}_F model to include the homology for S, L modules related by k given in Ciobanu
250 et al. (2009). The displacements are quantifiable by fractional shifts between reflections in the derived
251 and basic structures (e.g., module '7' derived from module '5', module '9' derived from module '7',
252 etc.). The adapted model stipulates that the distance between the two brightest reflections, about the
253 middle of d_{sub}^* , equals $i \cdot d_N^*$ only when the shift at this position is minimal (equal to $1/N_b$; N_b =layers
254 in the basic structure).

255 A correlation between electron diffractions and chemical modules for a series group of phases is
256 typical of mixed layer compounds (Amelinckx et al. 1989). If we use the model with blocks of constant
257 width, as in the “Mod2 and 5” model of Imamov and Semiletov (1971) and Shelimova et al. (2000), the
258 number of component modules cannot be correlated with the modulation along d_{sub}^* . For example,
259 tsumoite would have $n=1$ and $m=2$, requiring three distinct modules instead of two (the ‘5’ and ‘7’
260 modules considered here).

261 DISCUSSION

262 Phase stability

263 An evaluation of phase stability for each of the seven phases uses formation energy relative to
264 chemical composition. The stability of related compounds can be assessed by the convex hull method of
265 Gibbs (1973), with recent DFT applications to complex metallic compounds (Ma et al. 2017). The phase
266 stability is assessed by the distance between calculated formation energy ΔE_f and the energy of the
267 convex hull E_{hull} :

$$268 \Delta E_{distance} = E_{hull} - \Delta E_f, \quad (2)$$

269 and those compounds plotting above the hull are considered unstable. We employ the model of Woodcox
270 et al. (2019) that stipulates a simple relationship between ΔE_f , the energy of phase E_{phase} and the energy
271 of composing atoms, in this case the energies of E_{Bi} and E_{Te} using the equation (3):

$$272 \Delta E_f = \frac{E_{phase} - pE_{Bi} - qE_{Te}}{p+q}, \quad (3)$$

273 where p or q represent the number of Bi and Te atoms in the unit cell (phase), respectively (Table 2).
274 Calculated ΔE_f for the seven relaxed structures (Table 5) are plotted relative to atom.% Te in Figure 10a.
275 The convex hull is defined by the lines between endmembers and the compound with minimum ΔE_f , in
276 our case, bismuth, tellurium, and Bi_2Te_3 (tellurobismuthite), respectively. The calculated ΔE_f values are
277 negative for all phases and show a quasi-linear relationship along the Bi_2Te_3 -Bi branch of the hull.

278 The alternative alloy approach to Bi-Te phases (Woodcox et al. 2019) gives another hull that plots
279 above the one obtained here (Figure 10a). In this approach, the Bi_2Te_3 -Te branch hosts two phases (BiTe_2
280 and $\text{BiTe}_{4.88}$) and the branch towards Bi hosts three phases corresponding to BiTe (tsumoite), Bi_2Te and
281 $\text{Bi}_{4.88}\text{Te}$. Our data show lower ground state energy for phases of the same composition and is thus more
282 plausible in terms of thermodynamic stability. This is also because our input structures are more
283 appropriate than the simple, Bi-Te alloy-type substitution used by Woodcox et al. (2019).

284 A second model for evaluation of phase stability was introduced by Park et al. (2021), using the
285 mixing energies of the 2- and 5-atom modules according to the formula,

$$286 \quad E_{\text{mixing}} = \frac{E_{\text{Total}}^{n\text{Bi}_2 \cdot m\text{Bi}_2\text{Te}_3} - nE_{\text{Total}}^{\text{Bi}_2} - mE_{\text{Total}}^{\text{Bi}_2\text{Te}_3}}{N_{\text{atom}}}, \quad (4)$$

287 where N_{atom} = total number of atoms in a given phase. In this case, the hull is determined between
288 endmembers Bi_2Te_3 (tellurobismuthite) and bismuth, rather than bismuth and tellurium. The diagram
289 obtained for the six phases using the relaxed structures when calculating E_{mixing} values for each compound
290 (Table 5, Figure 10b) shows Bi_4Te_3 (pilsenite) as the minimum of the hull (Figure 10b). The energy for
291 each compound represents the ground state energy (E_0 in Table 3). The other compounds plot below the
292 branch between pilsenite and bismuth, indicating they are stable. BiTe (tsumoite) plots slightly above the
293 branch towards Bi_2Te_3 . However, the distance between the point and the hull is ~ 1.400 meV/atom, a
294 small offset indicating that tsumoite may be stable.

295 Park et al. (2021) calculate E_{mixing} for the nine phases defined as superstructures in Bos et al. (2007)
296 but using lattice parameters (a and c) from previous experimental studies. Park et al. (2021) obtained a
297 hull centered on Bi_2Te , rather than pilsenite as the minimum E_{mixing} point (Figure 10b). Except for
298 hedleyite, all the other five intermediate phases plot above the hull. Nonetheless, Park et al. (2021)
299 considered these phases as stable since the distance to the hull is within a cutoff of ~ 4.500 meV/atom.
300 We point at the significant differences between the results of Park et al. (2021) and our own, particularly

301 when comparing the same compounds, Bi₇Te₃ (hedleyite), Bi₂Te, and BiTe (tsumoite). We consider that
302 the energy differences are due to the lattice parameters used, which were fixed lattice parameter values
303 in Park et al. (2021) rather than obtained as the result of structure relaxation as in our study. Our data
304 show a better fit to the convex hull and are therefore more credible in terms of energetic stability.

305 Following the ideas of Park et al. (2021) that intermediate compounds in a modular series can be
306 obtained by mixing energies of the constituent units, we formulate the energy of mixing using the
307 accretional model as follows:

$$308 \quad E_{\text{mixing}} = \frac{S \cdot E_{\text{Total}}^{\text{Bi}_{2k}\text{Te}_3} + L \cdot E_{\text{Total}}^{\text{Bi}_{2(k+1)}\text{Te}_3} - S \cdot E_{\text{Total}}^{\text{Bi}_{2k}\text{Te}_3} - L \cdot E_{\text{Total}}^{\text{Bi}_{2(k+1)}\text{Te}_3}}{N_{\text{atom}}}. \quad (5)$$

309 Applying this to the three double module phases (S=1, L=1), we obtained $E_{\text{mixing}}=1.420$ meV/atom for
310 tsumoite (5.7), -0.040 meV/atom for Bi₅Te₃ (7.9), and -0.020 meV/atom for hedleyite (9.11), values very
311 close to zero. This implies that mixing between the incremental modules is close to ideal. Further
312 calculation for other intermediate phases (S>1, L>1) would test this statement.

313 **The γ - d_{sub} relationship: where does the series end?**

314 The “Mod2 and 5” model of Imamov and Semiletov (1971) and Shelimova et al. (2000) is popular
315 because it allows the separation of two blocks with different thermoelectric properties and electronic
316 band structures (e.g., Bos et al. 2007; 2012; Park et al. 2021). In this model, if m=0, bismuth becomes
317 the end member of the series. This is, however, impossible in the mixed layer compound model, or the
318 homologous series described by the accretional modules (Frangis et al. 1989; Ciobanu et al. 2009), in
319 which Te will always be part of the component modules. This implies the end of the series is close to but
320 never meets native bismuth.

321 The incremental decrease in d_{sub} across the series (Figure 2b, c) shows the size of this interval
322 moves towards a constant value for phases within the compositional range ~45 to 27 atom.% Te. A better
323 description of d_{sub} across the series is obtained using γ modulation (Figure 11). The fitted curve shows

324 that d_{sub} becomes a *de facto* constant of ~ 1.973 Å from $\text{Bi}_{20}\text{Te}_3$ ($k=10$) onwards, up to $\text{Bi}_{100}\text{Te}_3$ ($k=50$),
325 for example. Taking the values for interatomic distances in native bismuth reported for $R\bar{3}m$ space for
326 temperatures between 4.2 K and 298 K we note that these are in a comparable range (1.966-1.977 Å;
327 Wyckoff, 1963; Schiferl and Barrett, 1969). The d_{sub} of Bi_7Te_3 (hedleyite) is at the upper limit whereas
328 d_{sub} for single module phases with $k \geq 4$ falls within the range reported for native bismuth.

329 The incremental decrease in d_{sub} corresponds to phases lacking Te-Te bonds, i.e., towards Bi-rich
330 compositions from Bi_8Te_9 , a phase with 5.7.7 module stack (Figure 12). Such behavior can be rationalized
331 in terms of the relative contributions of Bi-Bi and Bi-Te bond lengths to the interlayer intervals across
332 the asymmetric unit cell along c (Figure 12). If we consider the ideal $d_0 = 2.000$ Å as a baseline, the
333 weighted, average values of Bi-Te bonds for each phase lead to an increase of d_{sub} whereas the Bi-Bi
334 bonds have the opposite effect. The total contribution (sum of the two calculated values for each phase)
335 shows a gentle slope from Bi_4Te_3 (pilsenite) to Bi_8Te_3 (Figure 12). The offset of d_{sub} decreases relative
336 to ideal d_0 and we predict it will stay constant for phases with $k \geq 10$.

337 Based on this consideration, we define three subgroups in terms of slope variation in d_{sub} , the
338 crystal-structural parameter that defines derivation of the series from the archetypal tetradymite structure:
339 (i) Bi_2Te_3 (tellurobismuthite) - Bi_8Te_9 – steep slope; (ii) Bi_8Te_9 - $\text{Bi}_{14}\text{Te}_3$ -gentle slope, and (iii) $\text{Bi}_{14}\text{Te}_3$ to
340 $\text{Bi}_{100}\text{Te}_3$, expanding to $\text{Bi}_{\infty}\text{Te}_3$ – almost flat (values $\ll 0.001$ Å). This implies that phases in range (iii),
341 i.e., $k > 7$, should be considered as disordered native bismuth rather than discrete members of the
342 tetradymite group. The structures of Bi-tellurides with $k > 7$ would be undistinguishable from native Bi
343 since they would have the same d_{sub} values. On the other hand, regular insertion of Te layers at such
344 large intervals into a bismuth matrix must be considered as very unlikely.

345 SUMMARY AND IMPLICATIONS

346

347 We have used density functional theory to obtain seven structures spanning the range Bi_2Te_3 - Bi_8Te_3
348 in the tetradymite homologous series with formula: $\text{S}[\text{Bi}_{2k}\text{Te}_3]\text{L}[(\text{Bi}_{2(k+1)}\text{Te}_3)]$; $k=1-4$. The structures
349 represent single modules [$\text{S}=1, \text{L}=0$; Bi_2Te_3 (tellurobismuthite), Bi_4Te_3 (pilsenite), Bi_2Te and Bi_8Te_3] and
350 double modules [$\text{S}=1, \text{L}=1$; BiTe (tsumoite), Bi_5Te_3 and Bi_7Te_3 (hedleyite)] within this range. The
351 relaxed structures show systematic increase in a and decrease in interlayer distance (d_{sub}). We observe
352 a sharp decrease in d_{sub} between tellurobismuthite (2.029 Å) and tsumoite (1.996 Å), followed by an
353 incremental decrease to Bi_8Te_3 (1.975 Å) with Bi content.

354 Models for the relaxed structures are used to show representative atomic arrangements, bonding, and
355 bond distances for the asymmetric unit cells. Variation in minimum and maximum bond lengths show
356 the series can be split into two parts, corresponding to structures with and without Te-Te bonds. The
357 latter are larger than the Bi-Bi and Bi-Te bonds, reflecting the variation in d_{sub} .

358 Scanning transmission electron microscopy simulations for the relaxed structures show a perfect
359 match with the atom models. Simulated electron diffractions and the reflection modulation along the c^*
360 show a good fit with published analytical data and the mixed-layer compound theory. The distribution
361 of reflections and their intensity variation along $d_{sub}^* = 1 / d_{sub}$ is described by two modulation vectors,
362 $\mathbf{q}=\gamma \cdot c_{sub}^*$ ($\gamma = 1.800-1.640$) and $\mathbf{q}_F=\gamma_F \cdot d_{sub}^*$ ($\gamma_F = 0.200-0.091$). The γ_F parameter underpins the S, L
363 building blocks as $\text{Bi}_{2k}\text{Te}_3$ and $\text{Bi}_{2(k+1)}\text{Te}_3$ for the double module structures instead of Bi_2 and Bi_2Te_3 ,
364 whereas γ relates to variation of the d_{sub} .

365 Density functional theory is also used to calculate the formation energies of the seven phases. This
366 shows that the phases in the range BiTe - Bi_8Te_3 lie on the Bi - Bi_2Te_3 - Te convex hull, implying they are
367 thermodynamically stable. However, further studies employing phonon calculations are required to
368 assess whether these phases can be experimentally synthesised.

369 We have built a model that describes the relationship between γ and d_{sub} . This allows us to predict
370 values for d_{sub} beyond the compositional range considered here, e.g., for k values of 5, 7, 10, or even

371 50. These values are within the analytical range of interlayer distance in native bismuth. The tetradymite
372 group is therefore constrained within the γ range between 1.800 (tellurobismuthite) to 1.588 (Bi₁₄Te₃),
373 beyond which γ no longer represents the tetradymite group but rather disordered native bismuth.

374 The present study carries implications for mineral nomenclature and classification as well as for the
375 technological applications of Bi-chalcogenides. The framework presented here allows for the prediction
376 of structures for any intermediate phases within the Bi-rich series of the tetradymite group. The same
377 approach can be extended to other series comprised of mixed-layer compounds, e.g., the aleksite series
378 (Cook et al. 2019) and other chalcogen-rich series within the tetradymite group, or REE-fluorocarbonates
379 of the bastnäsite-synchysite group (Ciobanu et al. 2017; 2022).

380 Applying the correct structural model should also help to understand the variation in the
381 thermoelectric or topological insulating properties of new compounds in the tetradymite group (Bos et
382 al., 2007; 2012; Goldsmid, 2014).

383 Crystal structures are also fundamental for calculation of thermodynamic properties, which in turn
384 places constraints on phase relations in the system Bi-Te (Mao et al., 2018; Hasanova et al., 2021). A
385 refined phase diagram for the system Bi-Te is important for synthesis of new compounds and for
386 understanding the strong association between Bi-tellurides and gold observed in nature.

387 **Deposit items:** The following are available online at [https:// xxxx/xxxxxx](https://xxxx/xxxxxx): cif files for seven structures.

388 ACKNOWLEDGMENTS AND FUNDING

389 This work was supported by the Australian Research Council through Linkage grant LP200100156
390 “Critical Minerals from Complex Ores”, co-supported by BHP Olympic Dam. We acknowledge access
391 to the Phoenix high-performance computer (HPC) at the University of Adelaide and thank Fabien Voisin
392 and Mark Innes for the assistance with VASP installation and HPC configuration. We appreciate the
393 constructive comments of two anonymous reviewers and editorial handling by Jianwei Wang.

394

REFERENCES CITED

- 395 Adenis, C., Langer, V., and Lindqvist, O. (1989) Reinvestigation of the structure of tellurium. *Acta*
396 *Crystallographica C: Crystal Structure Communications*, 45, 941-942.
- 397 Amelinckx, S., Van Tendeloo, G., Van Dyck, D., and Van Landuyt, J. (1989) The study of modulated
398 structures, mixed layer polytypes and 1-D quasi-crystals by means of electron microscopy and
399 electron diffraction. *Phase Transitions*, 16, 3-40.
- 400 Atuchin, V.V., Gavrilova, T.A., Kokh, K.A., Kuratieva, N.V., Pervukhina, N.V., and Surovtsev, N.V.
401 Structural and vibrational properties of PVT grown Bi_2Te_3 microcrystals. *Solid State*
402 *Communications*, 152, 1119-1122.
- 403 Birch, F. (1947). Finite elastic strain of cubic crystals. *Physical Review*, 71, 809.
- 404 Blöchl, P.E. (1994) Projector augmented-wave method. *Physical Review B*, 50, 17953.
- 405 Bos, J.W.G., Zandbergen, H.W., Lee, M.H., Ong, N.P., and Cava, R.J. (2007) Structures and
406 thermoelectric properties of the infinitely adaptive series $(\text{Bi}_2)_m(\text{Bi}_2\text{Te}_3)_n$. *Physical Review B*, 75,
407 195203.
- 408 Bos, J.W.G., Fauchaux, F., Downie, R.A., and Marcinkova, A. (2012) Phase stability, structures and
409 properties of the $(\text{Bi}_2)_m(\text{Bi}_2\text{Te}_3)_n$ natural superlattices. *Journal of Solid State Chemistry*, 193, 13–18.
- 410 Cheng, W., and Ren, S.F. (2011) Phonons of single quintuple Bi_2Te_3 and Bi_2Se_3 films and bulk materials.
411 *Physical Review B*, 83, 094301.
- 412 Ciobanu, C.L., Pring, A., Cook, N.J., Self, P., Jefferson, D., Dima, G.I., and Melnikov, V. (2009)
413 Chemical-structural modularity in the tetradymite group: A HRTEM study. *American Mineralogist*,
414 94, 517-534.
- 415 Ciobanu, C.L., Birch, W.D., Cook, N.J., Pring, A., and Grundler, P.V. (2010) Petrogenetic significance
416 of Au-Bi-Te-S associations: the example of Maldon, Central Victorian gold province, Australia.
417 *Lithos*, 116, 1-17.

- 418 Ciobanu, C.L., Kontonikas-Charos, A., Slattery, A., Cook, N.J., Ehrig, K., and Wade, B.P. (2017) Short-
419 range stacking disorder in mixed-layer compounds: a HAADF STEM study of bastnäsite-parisite
420 intergrowths. *Minerals*, 7, 227.
- 421 Ciobanu, C.L., Slattery, A.D., Cook, N.J., Wade, B.P., and Ehrig, K. (2021) Bi_8Te_3 , the 11-atom layer
422 member of the tetradymite homologous series. *Minerals*, 11, 980.
- 423 Ciobanu, C.L., Cook, N.J., Slattery, A., Ehrig, K., and Liu, W.Y. (2022) Nanoscale intergrowths in the
424 bastnäsite-synchysite series record transition towards thermodynamic equilibrium. *MRS Bulletin*,
425 47, 250-257.
- 426 Cook, N.J., Ciobanu, C.L., Wagner, T., and Stanley, C.J. (2007) Minerals of the system Bi-Te-Se-S
427 related to the tetradymite archetype: Review of classification and compositional variation. *Canadian*
428 *Mineralogist*, 45, 665–708.
- 429 Cook, N.J., Ciobanu, C.L., Spry, P.G., Voudouris P., and the participants of IGCP-486 (2009)
430 Understanding gold-(silver)-telluride-(selenide) mineral deposits, *Episodes*, 32, 249-263.
- 431 Cook, N.J., Ciobanu, C.L., Liu, W., Slattery, A., Wade, B.P., Mills, S.J., and Stanley, C.J. (2019)
432 Polytypism and polysomatism in mixed-layer chalcogenides: Characterization of $\text{PbBi}_4\text{Te}_4\text{S}_3$ and
433 inferences for ordered phases in the aleksite series. *Minerals*, 9, 628.
- 434 Cook, N.J., Ciobanu, C.L., Slattery, A., Wade, B.P., and Ehrig, K. (2021) The mixed-layer structures of
435 ikunolite, laitakarite, joséite-B and joséite-A. *Minerals*, 11, 920.
- 436 Feutelais, Y., Legendre, B., Rodier, N., and Agafonov, V. (1993) A study of the phases in the bismuth–
437 tellurium system. *Materials Research Bulletin*, 28, 591-596.
- 438 Frangis, N., Kuypers, S., Manolikas, C., Van Tendeloo, G., Van Landuyt, J., and Amelinckx, S. (1990)
439 Continuous series of one-dimensional structures in compounds based on M_2X_3 (M= Sb, Bi; X= Se,
440 Te). *Journal of Solid State Chemistry*, 84, 314-334.

- 441 Gibbs, J.W. (1973) A Method of Geometrical Representation of the Thermodynamic Properties of
442 Substances by Means of Surfaces. Transactions, Connecticut Academy, 2, 382-404.
- 443 Goldsmid, H.J. (2014) Bismuth telluride and its alloys as materials for thermoelectric generation.
444 Materials, 7, 2577-2592.
- 445 Grimme, S., Antony, J., Ehrlich, S., and Krieg, H. (2010) A consistent and accurate ab initio
446 parametrization of density functional dispersion correction (DFT-D) for the 94 Elements H-Pu.
447 Journal of Chemical Physics, 132,154104.
- 448 Hasanova, G.S., Aghazade, A.I., Imamaliyeva, S.Z., Yusibov, Y.A., and Babanly, M.B. (2021)
449 Refinement of the Phase Diagram of the Bi-Te System and the Thermodynamic Properties of Lower
450 Bismuth Tellurides. JOM, 73, 1511-1521.
- 451 Hohenberg, P., and Kohn, W. (1964) Inhomogeneous electron gas. Physical Review, 136, B864.
- 452 Imamov, R.M., and Semiletov, S.A. (1971) Crystal structure of the phases in the systems Bi-Se, Bi-Te
453 and Sb-Te. Soviet Physics Crystallography, 15, 845-850.
- 454 Kohn, W., and Sham, L.J. (1965) Self-consistent equations including exchange and correlation effects.
455 Physical Review, 140, A1133.
- 456 Kresse, G., and Furthmüller, J. (1996). Efficient iterative schemes for ab initio total-energy calculations
457 using a plane-wave basis set. Physical Review B, 54, 11169.
- 458 Kresse, G., and Joubert, D. (1999). From ultrasoft pseudopotentials to the projector augmented-wave
459 method. Physical Review B, 59, 1758.
- 460 Lange, P.W. (1939) Ein vergleich zwischen Bi_2Te_3 und $\text{Bi}_2\text{Te}_2\text{S}$. Naturwissenschaften, 27 133-134
- 461 Lind, H., and Lidin, S. (2003) A general structure model for Bi–Se phases using a superspace formalism.
462 Solid State Science, 5, 47-57.

- 463 Ma, J., Hegde, V.I., Munira, K., Xie, Y., Keshavarz, S., Mildebrath, D.T., Wolverton, C., Ghosh, A.W.,
464 and Butler, W.H. (2017) Computational investigation of half-Heusler compounds for spintronics
465 applications. *Physical Review B*, 95, 024411.
- 466 Mao, C., Tan, M., Zhang, L., Wu, D., Bai, W., and Liu, L. (2018) Experimental reinvestigation and
467 thermodynamic description of Bi-Te binary system. *Calphad*, 60, 81-89.
- 468 Medlin, D., Erickson, K., Limmer, S., Yelton, W., and Siegal, M.P. (2014) Dissociated dislocations in
469 Bi_2Te_3 and their relationship to seven-layer Bi_3Te_4 defects. *Journal of Material. Science*, 49, 3970–
470 3979.
- 471 Murnaghan F.D. (1944) The compressibility of media under extreme pressures. *Proceedings National*
472 *Academy of Science*, 30, 244-247.
- 473 Nabok, D., Tas, M., Kusaka, S., Durgun, E., Friedrich, C., Bihlmayer, G., Blügel, S., Hirahara, T., and
474 Aguilera, I. (2022) Bulk and surface electronic structure of Bi_4Te_3 from GW calculations and
475 photoemission experiments. *Physical Review Materials*, 6, 034204.
- 476 Nakajima, S. (1963) The crystal structure of $\text{Bi}_2\text{Te}_{3-x}\text{Se}_x$. *Journal of Physics and Chemistry of Solids*, 24,
477 479-485.
- 478 Nakayama, A., Einaga, M., Tanabe, Y., Nakano, S., Ishikawa, F., and Yamada, Y. (2009). Structural
479 phase transition in Bi_2Te_3 under high pressure. *High Pressure Research*, 29, 245-249.
- 480 Pack, J.D., and Monkhorst, H.J. (1977) "Special points for Brillouin-zone integrations"—a reply.
481 *Physical Review B*, 16, 1748.
- 482 Palmer, D.C. (2015). Visualization and analysis of crystal structures using CrystalMaker software.
483 *Zeitschrift für Kristallographie-Crystalline Materials*, 230, 559-572.
- 484 Park, S., Ryu, B., and Park, S. (2021) Structural Analysis, Phase Stability, Electronic Band Structures,
485 and Electric Transport Types of $(\text{Bi}_2)_m(\text{Bi}_2\text{Te}_3)_n$ by Density Functional Theory Calculations. *Applied*
486 *Science*, 11, 11341.

- 487 Perdew, J.P., Burke, K., and Ernzerhof, M. (1996). Generalized gradient approximation made simple.
488 Physical Review Letters, 77, 3865.
- 489 Perdew, J.P., Ruzsinszky, A., Csonka, G.I., Vydrov, O.A., Scuseria, G.E., Constantin, L.A., Zhou, X.
490 and Burke, K. (2008) Restoring the Density-Gradient Expansion for Exchange in Solids and
491 Surfaces. Physical Review Letters, 100, 136406.
- 492 Shelimova, L.E., Karpinsky, O.G., Kosyakov, V.I., Shestakov, V.A., Zemskov, V.S., and Kuznetsov,
493 F.A. (2000) Homologous series of layered tetradymite-like compounds in Bi-Te and GeTe-Bi₂Te₃
494 systems. Journal of Structural Chemistry, 41, 81–87.
- 495 Schiferl, D., and Barrett, C.S. (1969) The crystal structure of arsenic at 4.2, 78 and 299 K. Journal of
496 Applied Crystallography, 2, 30-36.
- 497 Stokes, H.T., and Hatch, D.M. (2005) FINDSYM: program for identifying the space-group symmetry of
498 a crystal. Journal of Applied Crystallography, 38, 237-238.
- 499 Vilaplana, R., Gomis, O., Manjón, F.J., Segura, A.; Pérez-González, E., Rodríguez-Hernández, P.,
500 Muñoz, A., González, J., Marín-Borrás, V., Muñoz-Sanjosé, V., and Drasar, C. (2011) High-pressure
501 vibrational and optical study of Bi₂Te₃. Physical Review B, 84, 104112.
- 502 Warren, H.V., and Peacock, M.A. (1945) Hedleyite, a new bismuth telluride from British Columbia, with
503 notes on wehrlite and some bismuth–tellurium alloys. University of Toronto Studies, Geology Series,
504 49, 55-69.
- 505 Woodcox, M., Young, J., and Smeu, M. (2019). Ab initio investigation of the elastic properties of
506 bismuth-based alloys. Physical Review B, 100, 104105.
- 507 Wyckoff, R.W.G. (1963) Crystal Structures, 2nd ed. Interscience Publishers, New York.
- 508 Yamana, K., Kihara, K., and Matsumoto, T. (1979) Bismuth tellurides BiTe and Bi₄Te₃. Acta
509 Crystallographica, B35, 147-149.

510 Zav'ylov, E.N., Begizov, V.D., and Nechelyustov, G.N. (1976) New data on hedleyite. Dokl. Acad. Nauk
511 SSSR, 230, 1439–1441 (in Russian).

512 Zurhelle, A.F., Deringer V.L., Stoffel, R.P., and Dronskowski, R. (2016) Ab initio lattice dynamics and
513 thermochemistry of layered bismuth telluride (Bi_2Te_3). Journal of Physics: Condensed Matter, 28,
514 115401.

515 **Figure captions**

516 **Figure 1.** Energy versus volume curves for the nine crystal structures corresponding to phases
517 as labelled, including elemental Bi and Te. Open black circles are total energies calculated from
518 DFT. Solid black curves are constructed by fitting the equation of state (1). The parameters
519 listed in Table 3 are obtained from the fitted curve. Native bismuth and tellurium are included
520 for the calculation of formation energy in equation (3).

521 **Figure 2.** Lattice parameters a (a) and d_{sub} (b,c) as a function of atom.% Te for the seven
522 studied phases. Data from literature (Table 1 and additional DFT studies) are indicated for
523 comparison. The value of d_{sub} for Bi_8Te_3 from Ciobanu et al. (2021) is included although is out
524 of the range calculated here. (a) The present data plots along a curve above the one refined from
525 literature (dashed line). The DFT data for tellurobismuthite is given with error bars. Note that
526 the mean value for previously published DFT data (Cheng and Ren 2011; Vilaplana et al., 2011;
527 Zurhelle et al., 2016) is midway between other published data and present study. The plot in (c)
528 is a close up of (b). Abbreviations: Hed—hedleyite; Pls—pilsenite; Tbs—tellurobismuthite;
529 Tsm—tsumoite.

530 **Figure 3.** Atom models (ball and stick to the left, atom filling to the right) for the relaxed
531 structures of the single module phases ($k=1-4$; $S=1$; $L=0$) as labelled viewed on $[11\bar{2}0]$ zone
532 axis. Atom-layer modules and their respective widths are marked by numbers at the top. The

533 sequence of atoms (red—Bi; green—Te) typifying the structure is shown along (hkl) planes, $i=-$
534 ($h+k$). Corresponding crystallographic information data files (cif.) included as Deposit items.

535 **Figure 4.** Atom models (ball and stick to the left, atom filling to the right) for the relaxed
536 structures of the double module phases ($k=1-3$; $S=1$; $L=1$) as labelled viewed on $[11\bar{2}0]$ zone
537 axis. Atom-layer modules and their respective widths are marked by numbers at the top. The
538 sequence of atoms (red—Bi; green—Te) typifying the structure is shown along (hkl) planes, $i=-$
539 ($h+k$). Corresponding crystallographic information data files (cif.) included as Deposit items.

540 **Figure 5.** Bonds and their respective lengths for atoms (red—Bi; green—Te) within the
541 asymmetric unit cell (viewed on $[11\bar{2}0]$ zone axis) for single module phases as labelled.
542 Maximum and minimum bond lengths are marked in red and tabulated for each phase to enable
543 an easier comparison. Projection of bond lengths along the c axis is marked for pilsenite, Bi_2Te
544 and Bi_8Te to illustrate the contribution of Bi-Bi and Bi-Te bonds to the d-subcell plotted on
545 Figure 12). Note that Te-Te bonds (with greatest length) are present only in tellurobismuthite.

546 **Figure 6.** Bonds and their respective lengths for atoms (red—Bi; green—Te) within the
547 asymmetric unit cell (viewed on $[11\bar{2}0]$ zone axis) for double module phases as labelled.
548 Maximum and minimum bond lengths are marked in red and tabulated for each phase to enable
549 an easier comparison.

550 **Figure 7.** Minimum and maximum bond lengths for all seven structures (data from Figures 5
551 and 6) plotted against atom.% Te. Differences between largest and smallest values are marked
552 adjacent to each diagram. (a, b) Minimum and maximum Bi-Te bonds. Note that all seven phases
553 contain such bonds. (c,d) Minimum Bi-Bi and maximum Bi-Bi and Te-Te bonds. Note that
554 tellurobismuthite lacks Bi-Bi bonds (in (c) and that pilsenite has only one Bi-Bi bond with value

555 within the range of minimum Bi-Bi bonds (not plotted on d). See text for additional details.

556 Abbreviations: Hed—hedleyite; Pls—pilsenite; Tbs—tellurobismuthite; Tsm—tsumoite.

557 **Figure 8.** STEM simulations (left) and electron diffraction (ED) patterns (right) obtained on
558 $[11\bar{2}0]$ zone axis for the relaxed structures corresponding to the single module phases as
559 labelled. Values for a , c and d_{sub} parameters correspond to those given in Table 4. The two
560 strips under each image show the d_{sub}^* interval cropped from ED patterns (area rectangle) and
561 computed intensity variation for reflections across this interval, displaying the number of
562 reflections and the two modulation vectors (as marked). The atom sequence corresponding to
563 each structure is marked by overlays on the images. Compare the simulations with the models
564 shown in Figure 3. Third order satellite reflections underpin the \mathbf{q} modulation along c^* (marked
565 by arrows and circles). Note that the simulations for unnamed Bi_2Te were performed using space
566 group $P1$ instead of $P\bar{3}m1$. See text for additional details.

567 **Figure 9.** STEM simulations (left) and electron diffraction (ED) patterns (right) obtained on
568 $[11\bar{2}0]$ zone axis for the relaxed structures corresponding to the double module phases as
569 labelled. Values for a , c and d_{sub} parameters correspond to those given in Table 4. The two
570 strips under each image show the d_{sub}^* interval cropped from ED patterns (area rectangle) and
571 computed intensity variation for reflections across this interval, displaying the number of
572 reflections and the two modulation vectors (as marked). The atom sequence corresponding to
573 each structure is marked by overlays on the images. Compare the simulations with models
574 shown in Figure 4. Third order satellite reflections underpin the \mathbf{q} modulation along c^* (marked
575 by arrows and circles). Note that the simulations for tsumoite were performed using space group
576 $P1$ instead of $P\bar{3}m1$.

577 **Figure 10.** Phase stability diagrams using the convex Hull approach. (a) Plot showing formation
578 energy from DFT calculations (Table 5) versus atom.% Te for the seven studied phases shown

579 in red (single modules) and green (double modules). A convex hull is defined by bismuth (Bi),
580 tellurobismuthite (Tbs) and tellurium (Te). The other six phases lie on the Bi-Tbs side (full line),
581 whereas the Tbs-Te side (marked by dashed line) is empty. The convex hull Bi-BiTe-Te
582 obtained from DFT calculations of Bi-Te alloys (marked as blue circles) (Woodcox et al. 2019)
583 is shown for comparison. (b) Plot showing energy mixing (equation 4 from Park et al. 2021)
584 versus $n/(n+m)$ using the Mod 2 and 5 model. The convex hull (red line) from our data (phases
585 as red circles) is between Tbs, pilsenite (Pls) and Bi. All phases, except tsumoite (Tsm) plot
586 underneath the Pls-Bi side, indicating stability. Tsumoite, plotting above the Pls-Tbs side, is
587 also likely stable given the distance to the hull (~ 1.400 meV/atom). In contrast, DFT data from
588 Park et al. (2021), using fixed lattice constants for the structures is defined by a Tbs-Bi₂Te-Bi
589 convex hull (data in blue). The distances to the hull for Tsm is larger than the fit obtained here
590 for relaxed structure of this compound. Abbreviation: Hed—hedleyite.

591 **Figure 11.** Model for the relation between d subcell and parameter γ showing that the
592 tetradymite series extends from tellurobismuthite to Bi₁₄Te₃ ($k=7$). The fitted curve ($d_{sub} =$
593 $6.457e-10 * \gamma^{31.15} + 1.973$) using calculated d subcell and γ values for the seven phases (in red)
594 allows prediction of d subcell for phases with higher k ($k=5, 7, 10, 50$ shown in green). The
595 slope of this curve has three domains with sharp, gentle, and flat trends, respectively (marked
596 as slopes 1-3). The boundary between slope 1 and 2 is marked by the first phase in which the
597 stacking sequence indicates a lack of Te-Te bonds (Bi₈Te₉, stack modules 5.7.7, shown in blue).
598 The boundary between slope 2 and 3 is marked by the composition Bi₁₄Te₃, the point on the
599 curve from where d-subcell becomes constant. Therefore, the phases in the slope 3 region should
600 be considered disordered native bismuth rather than compounds from the tetradymite series.
601 Interval of analytical data for interlayer distance in native bismuth in yellow.

602 **Figure 12.** Contribution of bond lengths to d-subcell for the three single module phases without
603 Te-Te bonds, pilsenite (Pls), Bi₂Te, and Bi₈Te₃. This can be seen as the difference between
604 weighted average bond lengths and reference d₀ which is taken as a baseline. The Bi-Te and Bi-
605 Bi bonds show opposing trends, and the total contribution of the two bond types decreasing from
606 Pls to Bi₈Te₃, in agreement with calculated d_{sub} values (Table 4).

Table 1. Background and crystal structures with published information on unit cell parameters.

Formula, Mineral name	Explicit formula	k	Module stacks	N ₁	Space Group	N total	c calc (Å)	Reference(s)	c (Å)	a (Å)	d subcell (Å)
Bi ₂ Te ₃ tellurobismuthite	Bi ₂ Te ₃	1	5	5	$R\bar{3}m$	15	30	<i>Atuchin et al. (2012)</i>	30.502	4.390	2.033
								Nakajima (1963)	30.497	4.386	2.033
								Feutelais et al (1993)	30.440	4.395	2.029
								Imamov and Semiletov (1971)	30.57	4.380	2.038
								^a Lange (1939)	30.423	4.369	2.028
BiTe tsumoite	Bi ₆ Te ₆	1	5.7	12	$P\bar{3}m1$	12	24	<i>Yamana et al. (1979)</i>	24.002	4.423	2.000
								Imamov and Semiletov (1971)	23.97	4.400	1.998
Bi ₄ Te ₃ pilsenite	Bi ₄ Te ₃	2	7	7	$R\bar{3}m$	21	42	<i>Yamana et al. (1979)</i>	41.888	4.451	1.995
								Imamov and Semiletov (1971)	41.870	4.43	1.994
Bi ₅ Te ₃ (unnamed)	Bi ₁₀ Te ₆	2	7.9	16	$R\bar{3}m$	48	96	<i>^bCiobanu et al. (2009)</i>	95.05	4.500	1.980
Bi ₂ Te (unnamed)	Bi ₆ Te ₃	3	9	9	$P\bar{3}m1$	9	18	<i>Bos et al. (2012)</i>	17.922	4.469	1.991
								<i>^cZav'ylov et al. (1976)</i>	17.805	4.4733	1.978
Bi ₇ Te ₃ hedleyite	Bi ₁₄ Te ₆	3	9.11	20	$R\bar{3}m$	60	120	<i>Imamov and Semiletov (1971)</i>	119.04	4.47	1.984
								Warren and Peacock (1945)	119	4.47	1.983
Bi ₈ Te ₃ (unnamed)	Bi ₈ Te ₃	4	11	11	$R\bar{3}m$	33	66	<i>^bCiobanu et al. (2021)</i>	63.000	4.400	1.909

^a structure given with rhombohedral axes as $a=b=c=10.45$ Å, $\alpha=\beta=\gamma=24.13^\circ$

^b S/TEM data

^c Zav'ylov et al. (1976) given as for hedleyite

The first listed for each phase (in italics) was used as input data for DFT structure calculations.

Table 2. Number of atoms and chemical formula units applied in each simulation box and KPOINTS grids chosen in the DFT computations for all seven Bi-tellurides structures, native bismuth and tellurium.

	Bi ₂ Te ₃	BiTe	Bi ₄ Te ₃	Bi ₅ Te ₃	Bi ₂ Te	Bi ₇ Te ₃	Bi ₈ Te ₃	Bi	Te
Number of atoms	15	12	21	48	9	60	33	6	3
Formula units	3	6	3	6	3	6	3	1	1
KPOINTS mesh	14x14x2	20x20x4	18x18x2	21x21x1	16x16x4	26x26x1	30x30x2	18x18x6	12x12x12

Table 3. Equation of state parameters fitted from the energy volume relation for the seven Bi-tellurides, native bismuth and tellurium. V_0 represents the equilibrium volume for each simulation cell, K_0 and K'_0 are the bulk modulus and its derivative. The V_0 and bulk modulus are compared with experimental and previously published calculations.

	E_0/atom (eV)	V_0/atom (Å ³)	K_0 (GPa)	K'_0	Ref.
Bi ₂ Te ₃	-3.96	34.50	33	6.3	This work
		33.93	41		[1]
BiTe	-4.00	34.51	40	5.0	This work
		33.89	41		[2]
Bi ₄ Te ₃	-4.03	34.60	40	5.2	This work
		34.22	41		[2]
Bi ₅ Te ₃	-4.05	34.74	39	5.2	This work
		33.18	41		[3]
Bi ₂ Te	-4.07	34.83	38	5.6	This work
		34.44	39		[4]
Bi ₇ Te ₃	-4.08	34.88	39	5.1	This work
		34.32	36		[5]
Bi ₈ Te ₃	-4.09	34.93	39	5.1	This work
		32.00	33		[3]
Bi	-4.19	35.49	36	5.7	This work
		35.07	38		[6]
Te	-3.41	33.30	29	5.8	This work
		33.94	48		[7]

[1] Atuchin et al. (2012)

[2] Yamana et al. (1979)

[3] Ciobanu et al. (2009)

[4] Bos et al. (2012)

[5] Imamov and Semiletov (1970)

[6] Schiferl and Barrett (1969)

[7] Adenis et al. (1989)

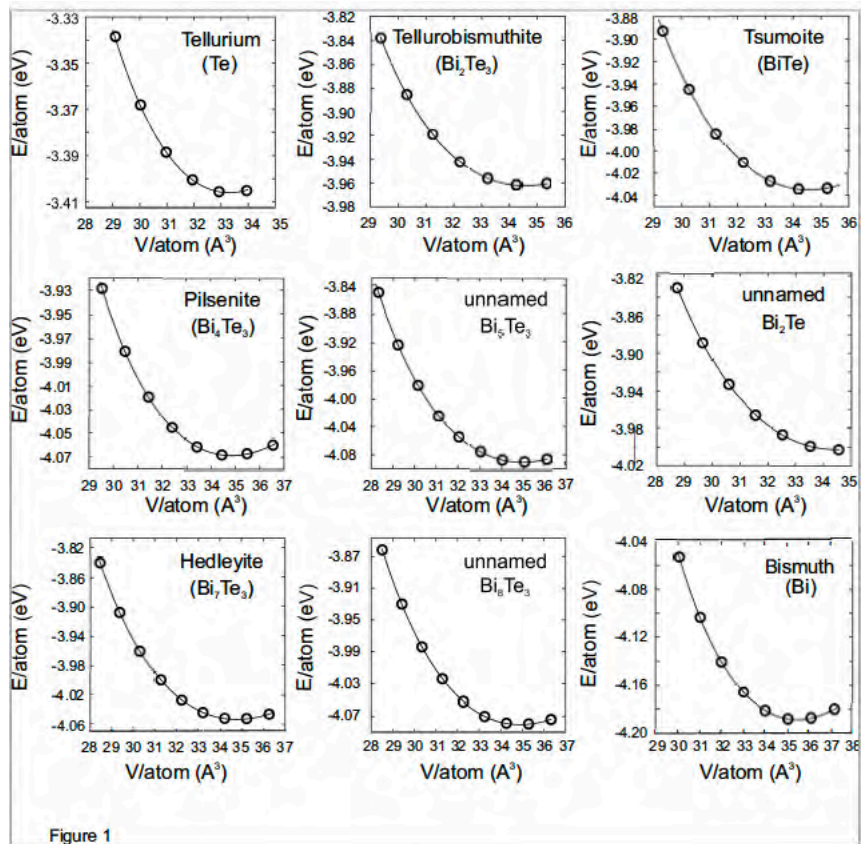
All bulk modulus data are from Woodcox et al. (2019)

Table 4. Calculated lattice constants a , c , volume, Z , and density for the seven relaxed Bi-telluride structures based on density functional theory. Values for d_{sub} are obtained from the c parameter and number of layers (N1) for each phase.

Name	Explicit formula, (N1)	Space group	a (Å)	c (Å)	Volume (Å ³)	Z	density (g/cm ³)	d_{sub} (Å)
Tellurobismuthite	Bi ₂ Te ₃ (5)	$R\bar{3}m$	4.431	30.433	517.561	3	7.7079	2.029
Tsumoite	Bi ₆ Te ₆ (12)	$P\bar{3}m1$	4.468	23.950	414.059	6	8.0995	1.996
Pilsenite	Bi ₄ Te ₃ (7)	$R\bar{3}m$	4.487	41.678	726.691	3	8.3552	1.985
Bi ₅ Te ₃	Bi ₁₀ Te ₆ (16)	$R\bar{3}m$	4.499	95.133	1667.607	6	8.5309	1.982
Bi ₂ Te	Bi ₆ Te ₃ (9)	$P\bar{3}m1$	4.508	17.811	313.463	3	8.6709	1.979
Hedleyite	Bi ₁₄ Te ₆ (20)	$R\bar{3}m$	4.514	118.613	2093.081	6	8.7863	1.977
Bi ₈ Te ₃	Bi ₈ Te ₃ (11)	$R\bar{3}m$	4.519	65.182	1152.771	3	8.8798	1.975

Table 5. DFT calculated formation energy (E_f) and energy of layer mixing (E_{mixing}) for seven phases from the tetradymite series. Equations (3) and (4) are given in the text.

	Bi ₂ Te ₃	BiTe	Bi ₄ Te ₃	Bi ₅ Te ₃	Bi ₂ Te	Bi ₇ Te ₃	Bi ₈ Te ₃
E_f (eV)	-242.533	-205.250	-181.048	-158.563	-141.000	-126.667	-114.909
E_{mixing} (meV/atom)	0.000	-3.139	-7.810	-6.979	-6.259	-5.400	-4.667



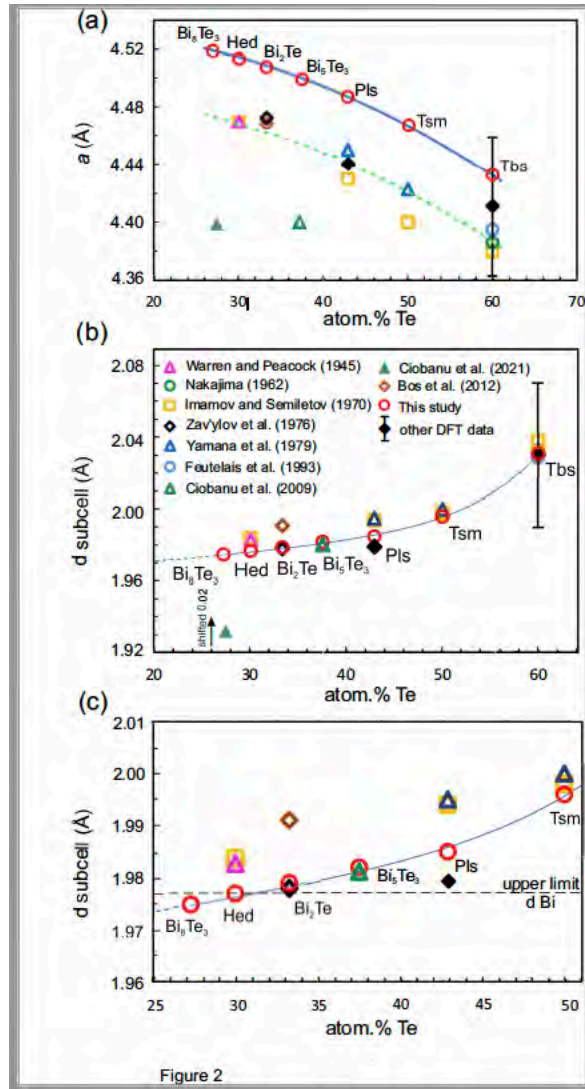
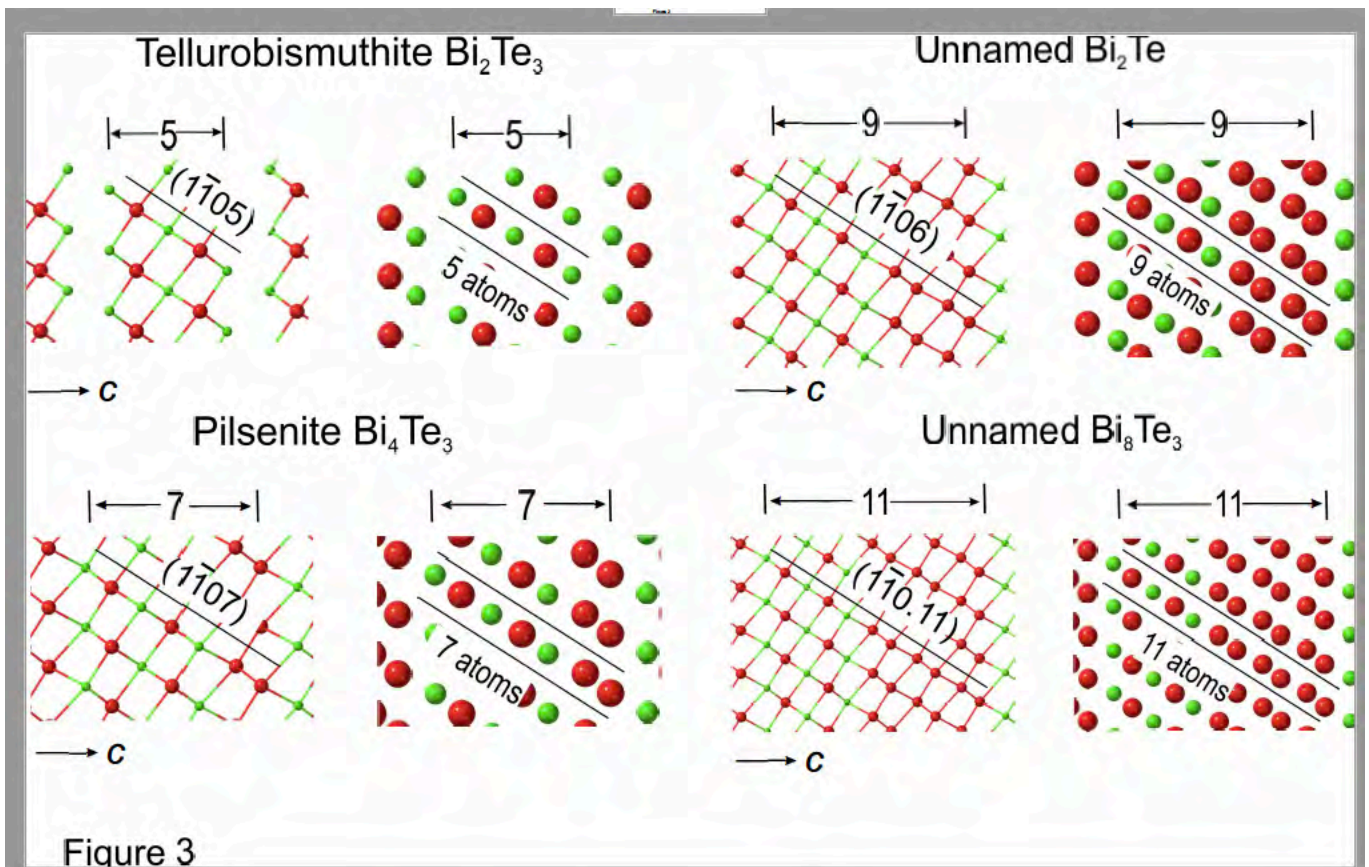
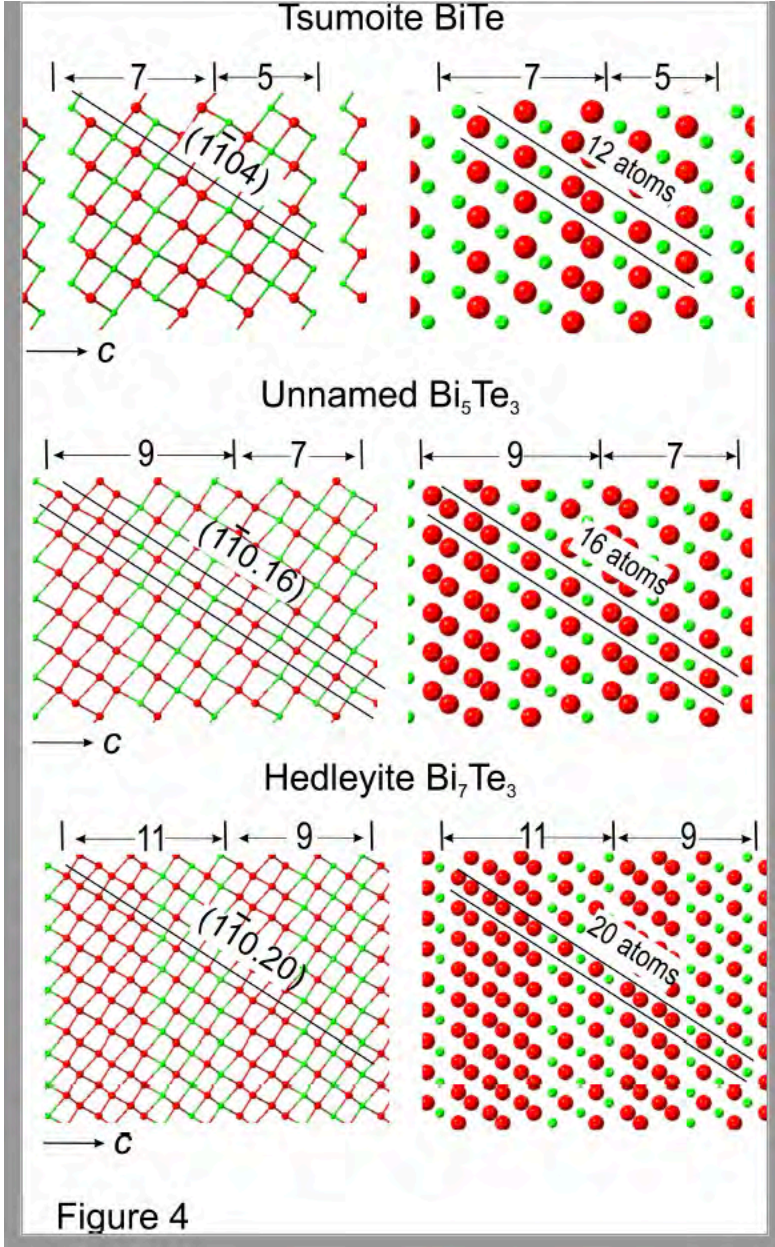


Figure 2





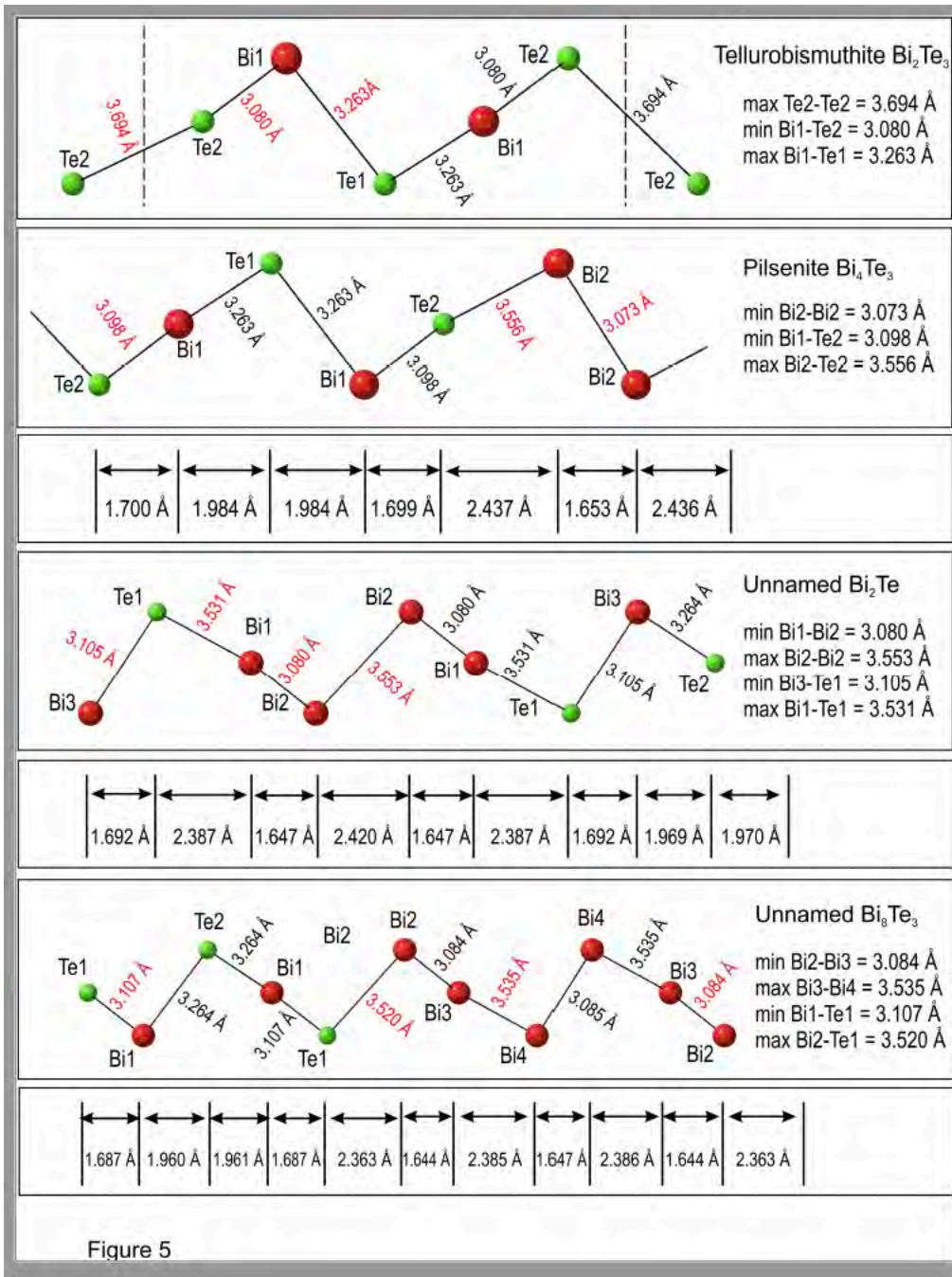


Figure 5

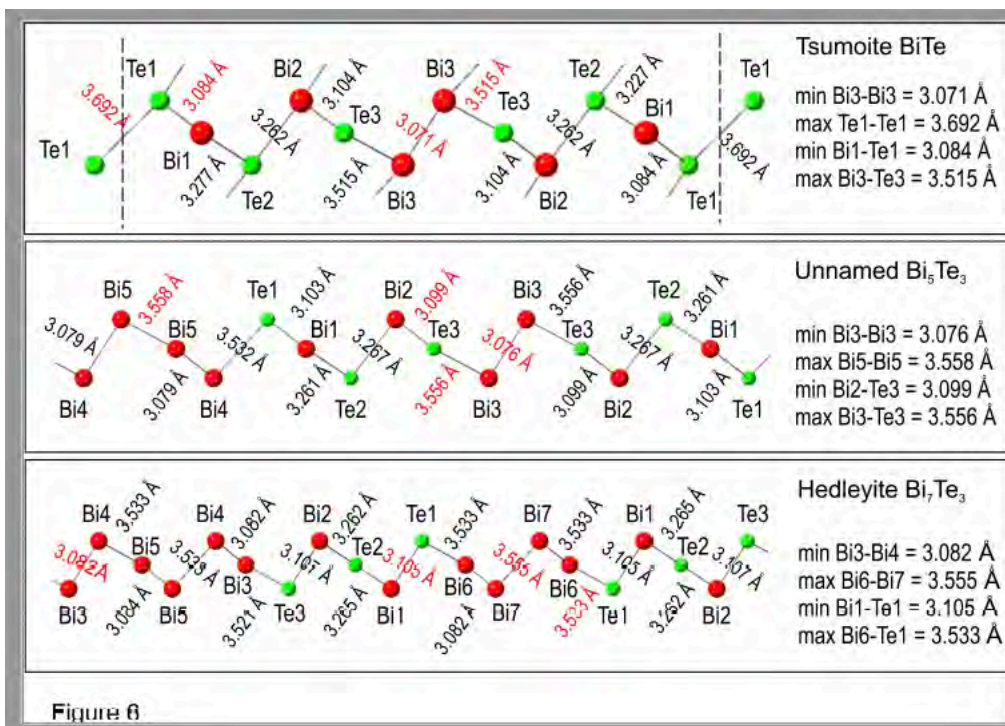


Figure 6

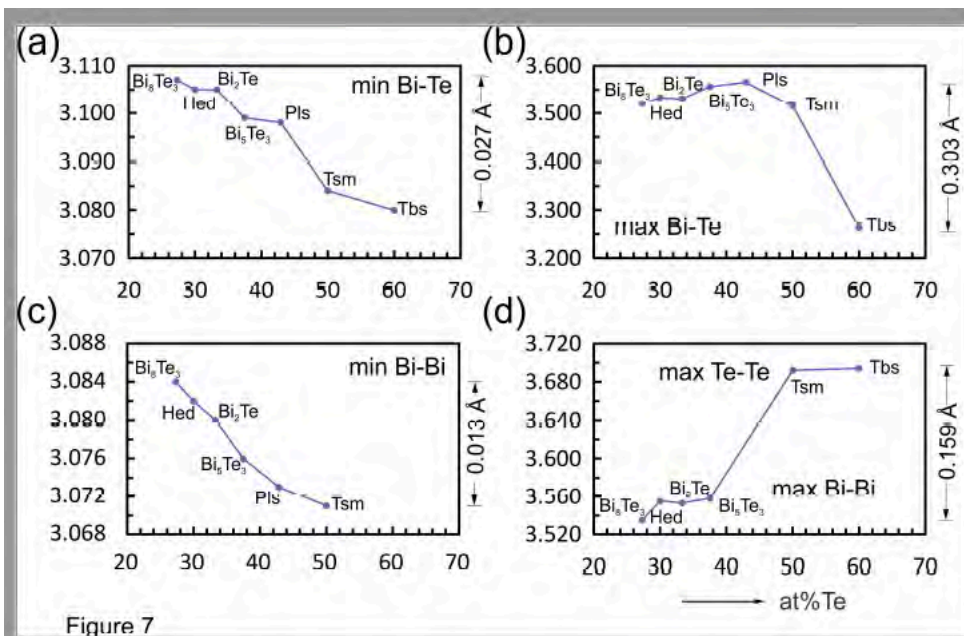


Figure 7

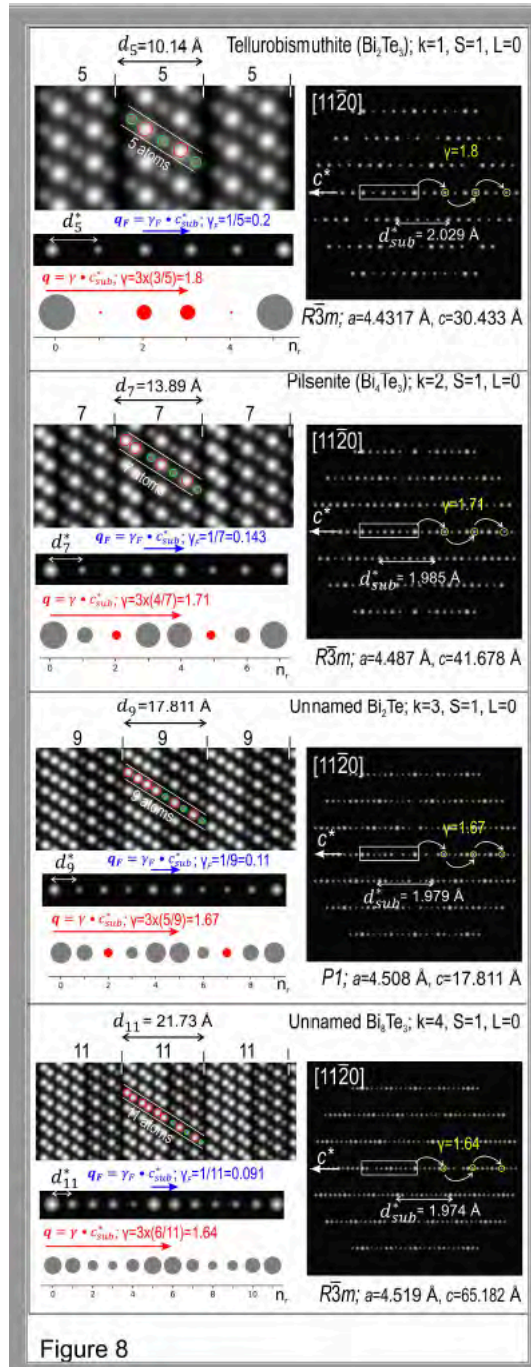


Figure 8

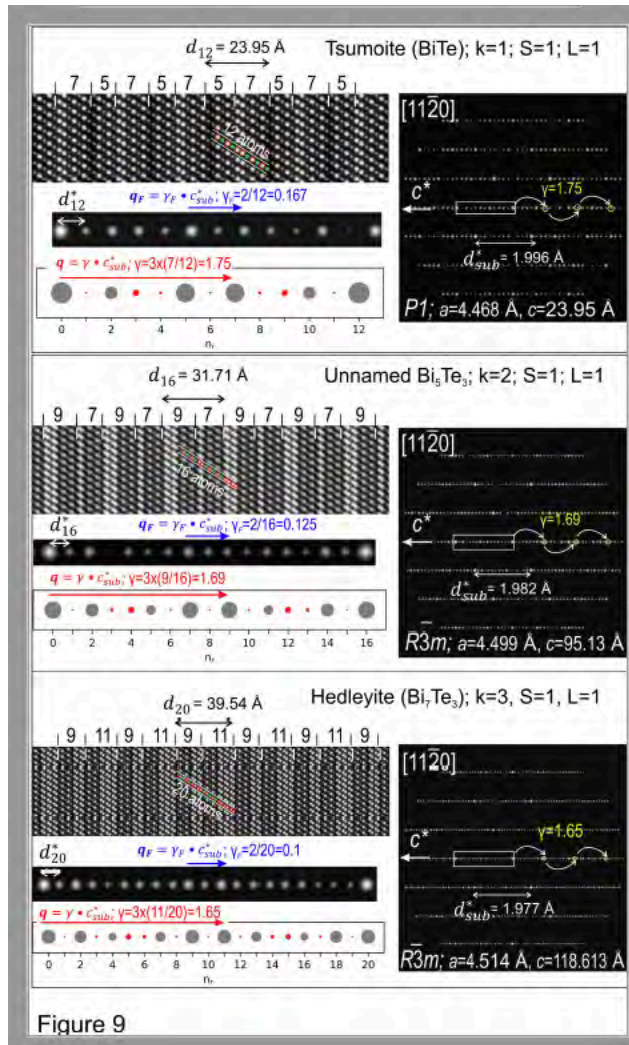


Figure 9

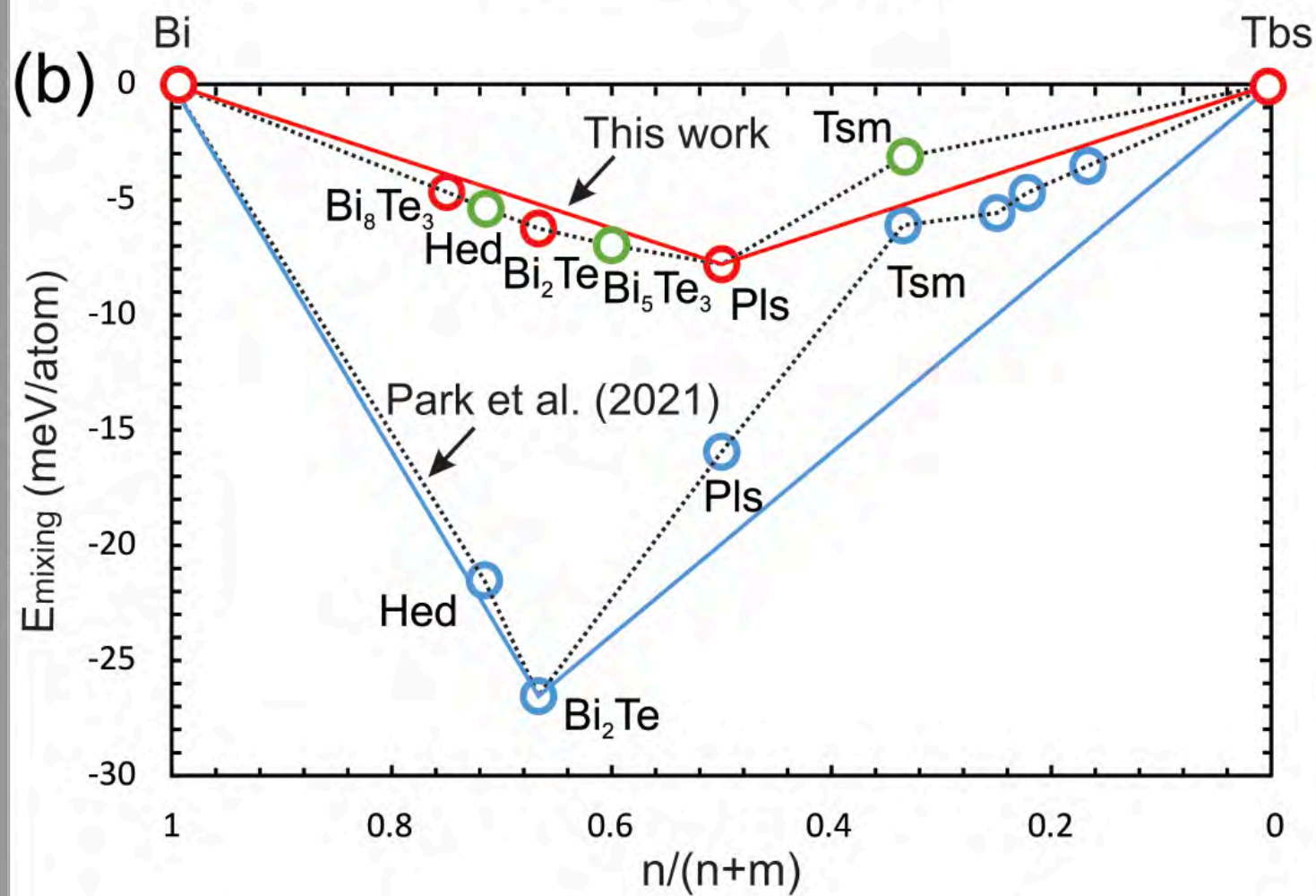
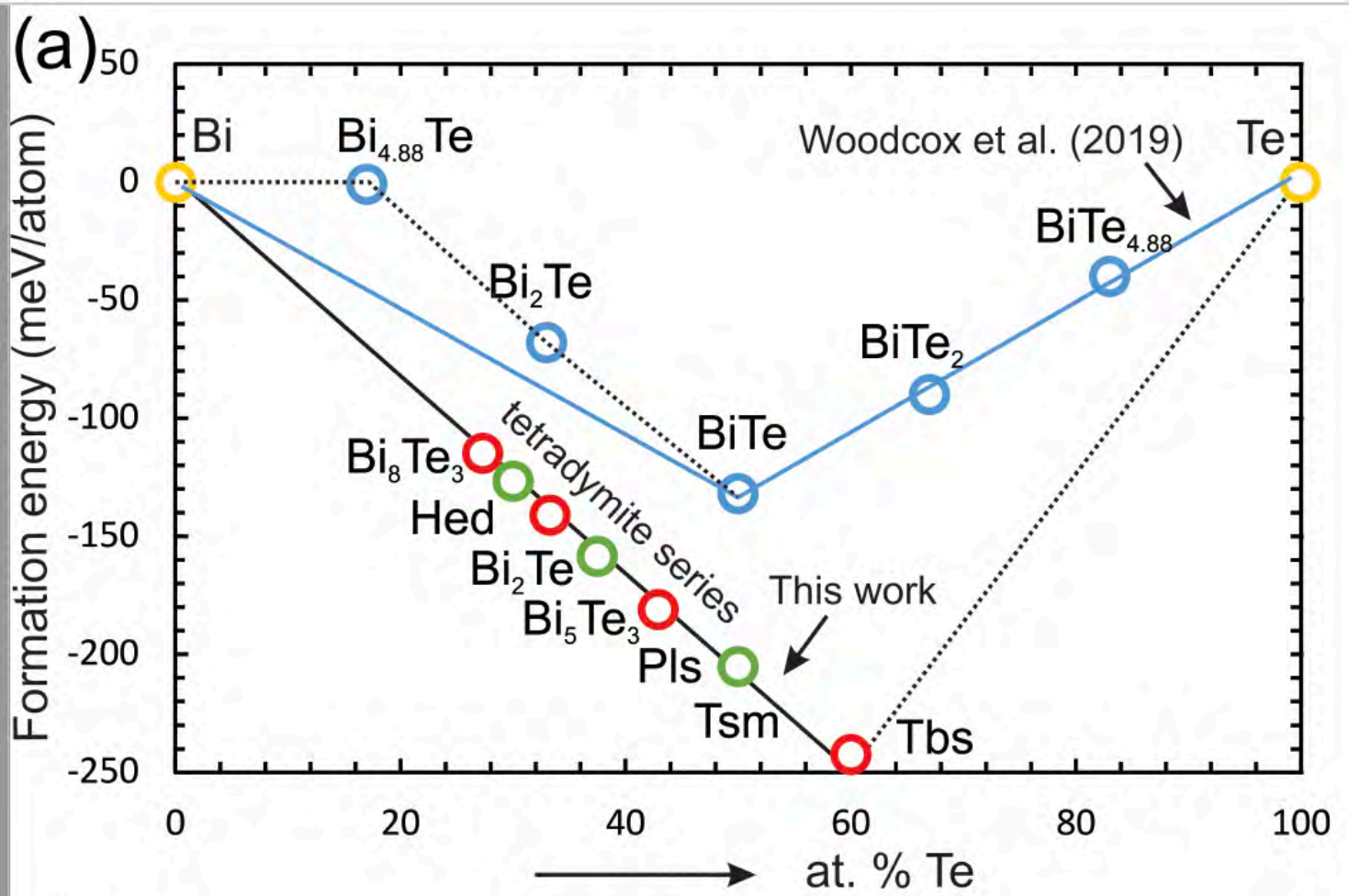


Figure 10

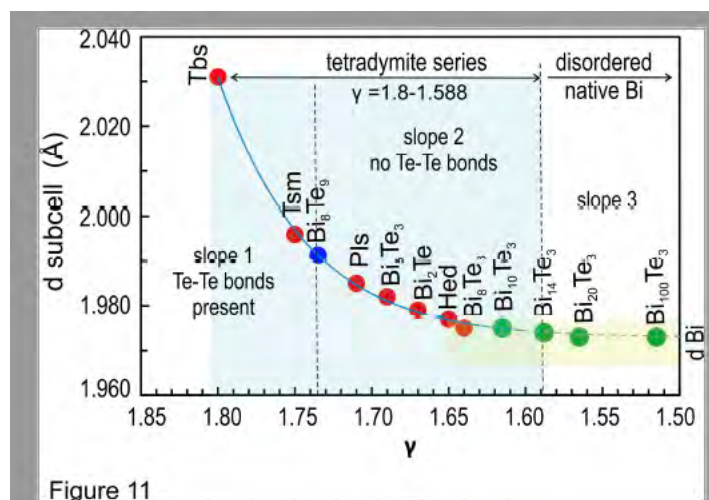


Figure 11

